

EMPIR 14IND02 - PlanarCal

Guidelines for the design of calibration substrates, including the suppression of parasitic modes for frequencies up to and including 325 GHz

Marco Spirito, **TUD**

Uwe Arz, **PTB**

Gia Ngoc Phung, Franz Josef Schmückle, Wolfgang Heinrich, **FVB**

Roger Lozar, **FhG**

EMPIR



The EMPIR initiative is co-funded by the European Union's Horizon 2020 research and innovation programme and the EMPIR Participating States

<https://planarcal.ptb.de>

July 2018

This Guide has been produced within the EURAMET project entitled *Microwave measurements for planar circuits and components*. More information about this collaborative research project can be found on the project's website <https://planarcal.ptb.de>.

Disclaimer

Any mention of commercial products within this Guide is for information only; it does not imply recommendation or endorsement by the partners in this project.

The views expressed in this Guide are those of the authors and of the EMPIR 14IND02 project team.

Acknowledgement of funding

The production of this Guide was funded by the European Metrology Programme for Innovation and Research (EMPIR). The EMPIR initiative is co-funded by the European Union's Horizon 2020 Research and Innovation Programme and the EMPIR Participating States.

Authorship

Preparation of this Guide was led by Marco Spirito of the Technical University of Delft (TUD), Delft (Netherlands) with extensive input from all the members involved of the EMPIR 14IND02 project team. The discussion and input of all the partners in the project and their colleagues are greatly appreciated.

Suggestion for the quotation of the references

Spirito, Marco ; Arz, Uwe ; Phung, Gia Ngoc ; Schmückle, Franz Josef ; Heinrich, Wolfgang ; Lozar, Roger. Guidelines for the design of calibration substrates, including the suppression of parasitic modes for frequencies up to and including 325 GHz : EMPIR 14IND02 – PlanarCal, 2018. Physikalisch-Technische Bundesanstalt (PTB).

DOI: <https://doi.org/10.7795/530.20190424A>

This document and all parts contained therein are protected by copyright and are subject to the Creative Commons user license CC by 4.0 (<https://creativecommons.org/licenses/by/4.0/>).



Guidelines for the design of calibration substrates, including the suppression of parasitic modes for frequencies up to and including 325 GHz

Deliverable participating Partners

TU Delft	Technische Universiteit Delft	Netherlands
PTB	Physikalisch-Technische Bundesanstalt	Germany
FhG	Fraunhofer-Gesellschaft zur Foerderung der angewandten Forschung e.V.	Germany
FVB	Forschungsverbund Berlin e.V.	Germany

Contents

Contents.....	4
1. Preface	5
2. Introduction	5
2.1. Multi-mode propagation.....	7
2.2. Boundary conditions (bounded-unbounded)	8
2.3. Characteristic impedance determination.....	9
3. Mode suppression.....	10
3.1. Structure optimization for coplanar waveguides.....	10
3.1.1 Influence of CPW ground width	11
3.1.2 Impact of ground-to-ground spacing	13
3.2 Probe topology	14
3.3 Chuck topology	17
3.4 Design guidelines related to the probe construction for coplanar waveguides	19
3.5 Thin-film Microstrip lines (TFMSL).....	22
3.6 Design guidelines related for thin-film microstrips.....	27
4. Example of custom designed TRL kit	28
Acknowledgements.....	30
Bibliography	30

1. Preface

The scope of this guideline is to make the reader aware of the constraints arising when attempting probe level calibration at higher frequencies, especially above 110GHz. The causes of generation of un-wanted radiation modes are first briefly described, and an approach to identify their impact on the calibration quality is provided to the reader with general first order guidelines. The report then describes the approaches that have been investigated and quantified as viable methods to reduce the generation of unwanted modes. Finally, an example of a custom built Thru Reflect Line (TRL) kit with suggestions on how to create the lines and the reflect conditions are given for illustrative purposes.

Finally, it is worth to mention that since the understanding, modelling and definition of solutions for mm-wave calibration is a relatively new research topic, this guide presents the derived knowledge of an ongoing work in the larger scientific community.

2. Introduction

The accuracy of S-parameter measurements of any device under test (DUT) is set, at the first order, by the quality of the Vector Network Analyzer (VNA) calibration. This is typically performed by measuring a certain number of known devices (i.e., the calibration standards). Depending on the specific calibration technique employed, the quality of the calibration is dependent on the accuracy with which the calibration standards are known/modelled.

For the interested reader a comprehensive description of calibration techniques can be found in [1]. When considering planar devices, for which wafer-probes need to be employed, it is common practice to perform a probe-level calibration (*first-tier*) using a low-loss substrate (i.e., alumina or fused silica), which can then be transferred to the environment in which the DUT is embedded.

To increase the DUT measurement accuracy, the test fixture (i.e., pad and interconnect lines) where the device is embedded can be further removed with a de-embedding step or a direct device level calibration [2].

Calibration techniques in which little knowledge of the standards is required, like Line Reflect Match (LRM) [3] and TRL [4], tend to be preferred when operating in the mm-wave frequency range (i.e., in the context of this document especially above 110GHz), since this reduces the calibration errors arising from the inaccuracy in the standard models.

Both TRL and LRM calibrations define the reference plane at the centre of the (non-zero) thru standard, and not at the probe tips, for this reason when referring to a first-tier (probe level) calibration a back shift on the calibration reference plane needs to be applied (note, that this will employ the knowledge of the transmission line electrical parameters).

The well-known relation between frequency and wavelength (λ), i.e., $\lambda=v/f$, where v is the phase velocity in the medium ($c/\sqrt{\epsilon_r}$), highlights the importance of referring to the electrical length of a medium rather than its mechanical one.

In simple words, as the frequency increases, assuming a fixed material thickness, a larger portion of the wave can be included in the dielectric slab, as shown in the sketch of Fig. 1 a). Moreover, also as the permittivity of the dielectric increases (larger ϵ_r), for a given frequency, a larger portion of the wave can

be included in the substrate Fig. 1 b). Both the mentioned cases (i.e., higher frequency and higher ϵ_r) can lead to wave radiation/reflection phenomena.

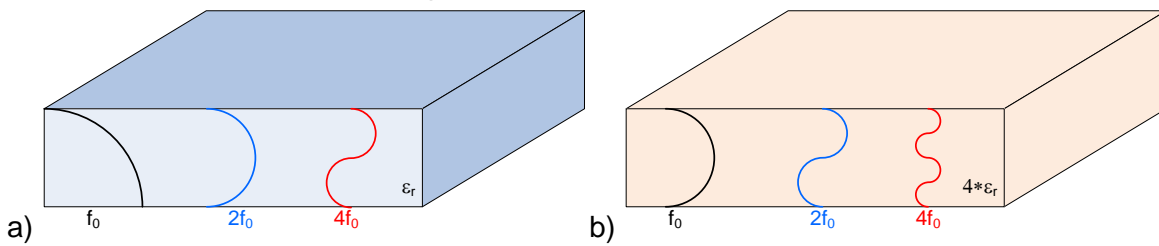


Fig. 1: Simplified sketch of the effect of wavelength reduction with frequency for a given substrate permittivity a), and for the same set of frequencies for a substrate with an higher (four times) permittivity b).

Commercially available calibration kits, employ only homogenous Coplanar Waveguides (CPW) transmission lines structures to perform the calibration procedure, since a width step in the line, would result in a discontinuity (modelled as a series reactance, as shown in Fig. 2 [5]), increasing the error when defining the reference plane at the probe tips, or requiring extra correction steps to remove the pad and step width effects.

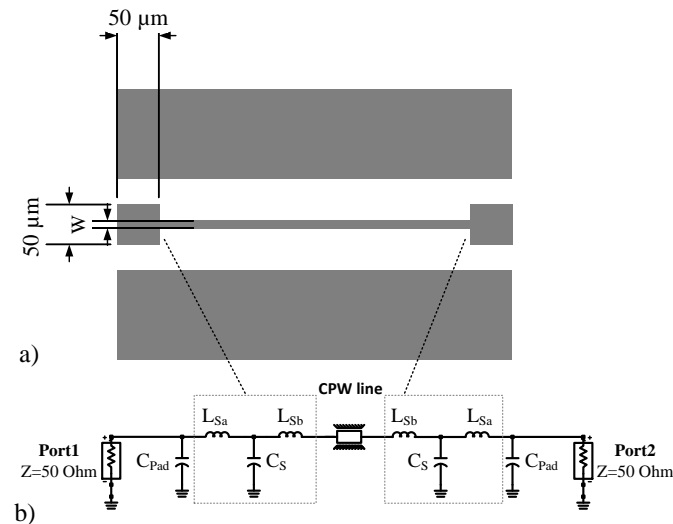


Fig. 2: a) top view of the CPW line sketch presenting a step width between the pad and the line, b) simulation setup for the thru employing a single shunt capacitance for modelling the pad, and the lumped model introduced in [6] for the pad-to-line transition.

Moreover, the probe landing area, often referred to as the scratch mark after touchdown and skating of the probe to reach the required (advised by the manufactures) over-travel to obtain a good (low) ohmic contact, does not scale with the operational frequency of the probe. In Fig. 3 the landing area for the same probe model from company #1 are shown for the WR10, WR5 and WR3 version, in Fig. 3 a), b) and c) respectively. Fig. 3 d) and e) presents the landing area for the WR3 model of probes produced from company #2 and company #3, respectively.

The illustrations in Fig. 3 are only qualitative and are not provided to represent the nominal response of the probes, but provide a visual justification to the fixed dimension of the signal line of the CPWs used in most of the commercially available calibration kits.

As a result, the high dielectric constant employed in commercially available substrates, with the large gaps in the CPW design (required to balance the L provided by the fixed line width and provide a $50\ \text{Ohm}$ nominal Z_0 of the line) leads to various unwanted modes being present in the lines used for probe level calibration in the frequency range above 110 GHz.

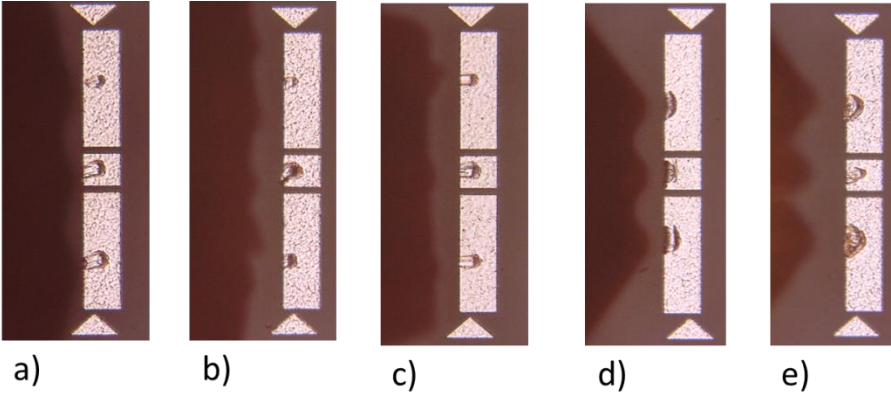


Fig. 3: Landing area of probe model from company #1 for the WR10 a), WR5 b) and WR3 c) frequency band, probe model from company #2 for the WR3 d) and probe model from company #3 for the WR3 e).

2.1. Multi-mode propagation

The different propagating modes supported by a CPW are qualitatively sketched in Fig. 4. The CPW mode characterized by opposite direction of the fields across the slots, represents the intended propagation mode and is often referred to as CPW differential mode. The CPW mode characterized by

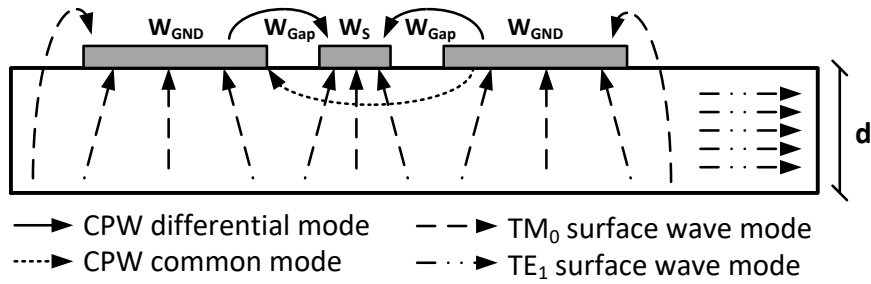


Fig. 4: Cross section of a CPW with finite ground planes, and sketches of the E field distributions of the first propagating modes supported.

in-phase direction of the field across the slots represents an unwanted radiating mode and is often referred to as CPW common mode.

The TM_n and TE_n modes are surface waves propagating along the dielectric slab, their cut off frequency is a function of the height, dielectric constant of the substrate and the bounding conditions. At the frequencies in which the lowest dispersive mode exhibits a propagation constant higher than the dominant CPW mode, the latter is not bounded anymore and energy leakage can occur from the nominal CPW mode to the un-wanted radiation mode. This critical frequency will depend on various parameters: substrate permittivity, height and boundary conditions. The boundary conditions will define the lower order dispersion mode (i.e., surface wave) that can propagate.

In the practical case of calibration substrates, two conditions are considered:

- 1) Metal chuck: this condition provides effectively a ground back plane to the CPW which will cancel the TE_0 mode for this configuration, the TM_0 is then the first dispersive mode. The critical frequency for this configuration was shown in [8], and is reported in eq. 1.

$$f_{Metal} = \frac{\arctan(\epsilon_r)}{\pi \cdot h \cdot \sqrt{2 \cdot \mu_0 \cdot \epsilon_0 \cdot (\epsilon_r - 1)}} \quad (1)$$

Where, ϵ_r represents the substrate permittivity, and h its height.

2) Dielectric chuck: when the calibration substrate is placed over a dielectric chuck presenting the same permittivity, the first unwanted mode to propagate is the TE_0 which will create leakage effects at frequencies above $f_{Dielectric}$, see eq. 2, as described in [8].

$$f_{Dielectric} = \frac{2}{W \cdot \sqrt{2 \cdot \mu_0 \cdot \epsilon_0 (\epsilon_r - 1)}} \quad (2)$$

Where W is the total width of the CPW line, including the ground planes. Both eq. 1 and eq. 2 show that the critical frequencies allowing leakage effects depends on the substrate permittivity (ϵ_r). In both cases the usage of a high permittivity material will lead to a lower value for the critical frequency where energy leakage will start to occur. In the bounded case eq. 1, the usage of thin substrates also shifts to higher frequencies the start of the leakage effect. It is important to note that eq. 2 represents an idealized case where no dielectric discontinuities exist, leaving the energy that has leaked to the unwanted mode to flow away from the structure.

Guideline #1

Compute the critical frequency (f_c) of the calibration substrate employed in the given configuration (i.e., metallic or dielectric chuck) and select those in which f_c is outside the calibration frequency or only occurs in the upper calibration range, to avoid excessive coupling of power to unwanted modes.

2.2. Boundary conditions (bounded-unbounded)

The effect of (i.e., error arising from) the presence of unwanted modes can be, to a first approximation, quantified by means of electro-magnetic (EM) simulations. The boundary conditions in a real environment will present effect comprised between the metal chuck condition (i.e., full reflection at the back side, providing a worst case condition Fig. 5 a) and the match/ open boundary condition (i.e., infinite medium at the back side, providing a best case condition Fig. 5 b).

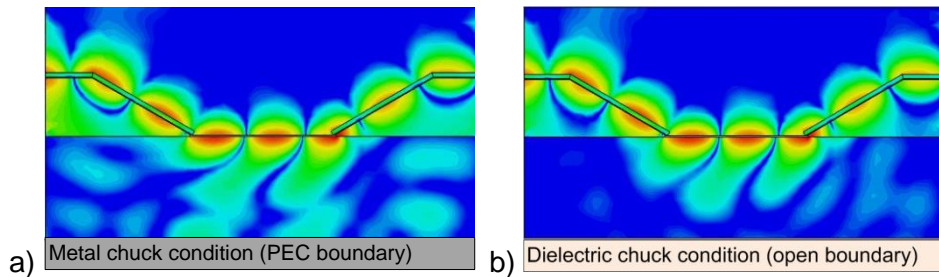


Fig. 5: Alumina substrate intensity of the E field shown in dB scale, using fixed scale range, at 200GHz, for the following lower boundary condition settings: a) perfect electrical conductor, b) radiation open (matching layer).

For this reason we can use the difference of the worst case bound metric [9], see eq. 3, in the two cases to provide a qualitative indication of the accuracy that the calibration on the given substrate can achieve.

$$WCB(f) = \max |S'_{ij}(f) - S_{ij}(f)| \quad (3)$$

To provide some information on the sensitivity of the calibration accuracy to the bounding conditions, we consider the WCB deviation computed as the distance between the metric in the two bounding conditions. This deviation is shown for both the Alumina and Fused Silica case in Fig. 6 (left axis). The peak to peak variation of the curve can be interpreted as the potential variation of the WCB due to boundary condition variations. While the metal chuck condition is an extremely pessimistic case, due to the common practice of ferrite interposer, Fig. 6 still provides information on the higher severity, in the calibration accuracy, of no perfect termination in high permittivity substrates.

Note, that the bound in eq. 3, needs to use the same normalization impedance for the S' and S matrices, moreover the bound will also incorporate the impact of the propagation of error through the chosen calibration procedure given the fact that corrected data are compared.

When reading the right axis of Fig. 6, the mean value of the WCB for the boundary match case (ideal) is presented for both calibration substrates. The increased (average) error in TRL calibrations on high permittivity substrates can be associated to the extremely complex modeling requirements (thus prone to errors) of the line parameters (i.e., Z_0) to properly account for the loss mechanism connected to higher order modes.

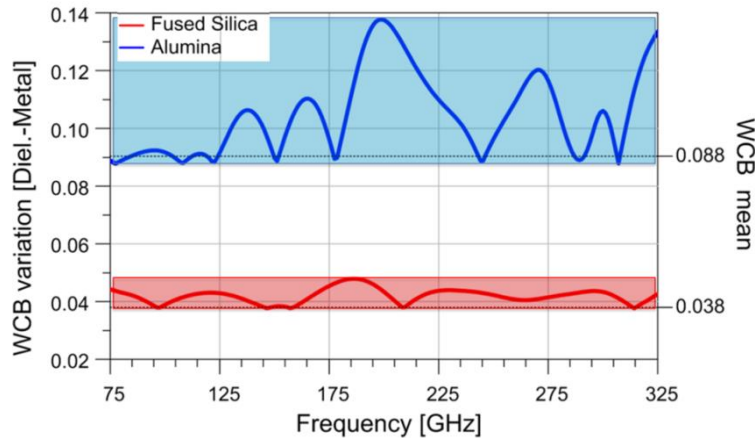


Fig. 6: Worst case bound differences between the match (dielectric) and PEC (metal) boundary conditions for both Alumina and Fused Silica substrates.

Guideline #2

The WCB difference between the ideal (match) and worst case (metal) boundary condition, extracted from the simulated response of the calibration structures, can be used to inform on the sensitivity of the calibration substrate to the real bounding condition employed.

2.3. Characteristic impedance determination

To properly describe the behaviour of the transmission lines used during the calibration process in both TRL and LRM procedures the characteristic impedance of the line needs to be properly defined.

The generalized equivalent circuit of a transmission line where multi-mode propagation is present can be represented as shown in Fig. 7.

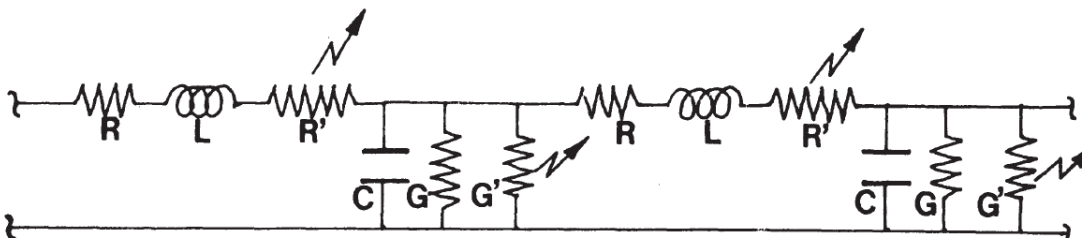


Fig. 7: Generalized equivalent circuit of a transmission line with distributed radiation, where R' and G' are respectively the series radiation resistance and the shunt radiation conductance per unit length [7].

The presence of the radiation resistance and conductance requires the usage of accurate modelling strategies to properly extract the real and imaginary part of the characteristic impedance of lines used in the calibration process.

Guideline #3

The following methods, among others, have been introduced in literature to properly account for the Z_0 of the line when radiation is present.

- Equation based modelling: In [8] conductor backed coplanar waveguide (CPW) with finite ground planes presenting dispersion and radiation properties are analyzed and modeled.
- Quasi-Analytical Tool: In [11] a software tool that allows for fast characterization of dynamic phenomena in a wide variety of transmission lines that include characteristic impedance, effective dielectric constant, and losses, such as radiation into space and surface waves is presented. The tool is available for free download on-line:
<http://terahertz.tudelft.nl/Research/project.php?id=74&ti=27>
- 3D EM FEM solver: In [5] a procedure to use 3D EM commercially available tools is presented to properly extract the Z_0 of lines where radiation phenomena are present.

In addition when surface roughness, which also impacts the Z_0 computation, needs to be included the model described in [10], can be employed.

3. Mode suppression

3.1. Structure optimization for coplanar waveguides

In the CPW case, typical questions refer to design rules on how the width of the CPW ground planes and the ground-to-ground spacing should be chosen in order to keep parasitic mode excitation to a minimum. This is discussed in the following. The presented results are supported by electromagnetic simulations and measurements. For EM simulation, the software tool MWS from CST is applied. The extracted simulated results are then compared to measurements in order to assess the validity of the simulation results. Analyzing the simulation results, design guidelines for calibration substrates can be derived, including the suppression of parasitic modes for mm-wave frequencies above 110 GHz.

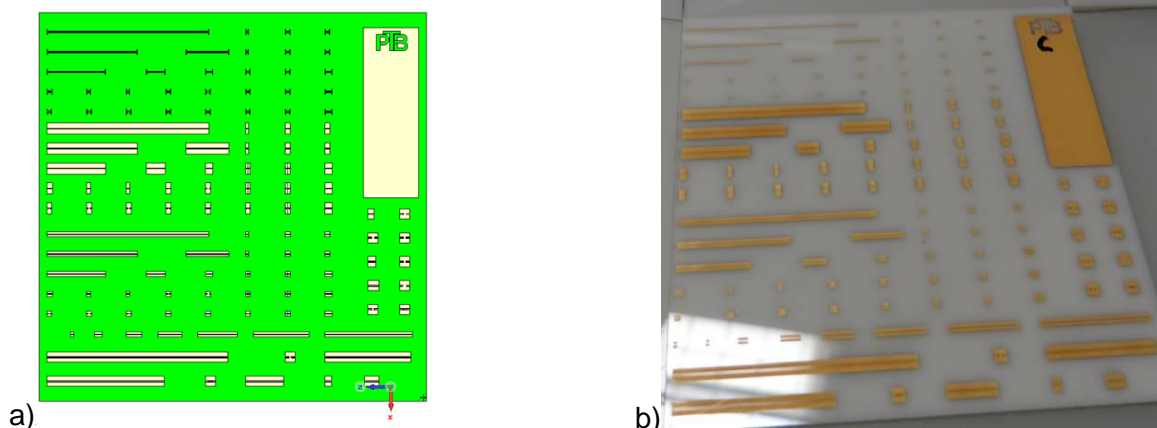


Fig. 8: Layout (a) and photograph (b) of the investigated wafer with 3 calibration sets of CPW lines with different ground width.

In order to perform the investigations a wafer based on the layout of [12], see Fig. 8 was manufactured for the Physikalisch-Technische Bundesanstalt (PTB) by Rohde & Schwarz (RuS). The wafer is designed to demonstrate these parasitic effects. Table 1 shows the CPW dimensions used.

The common parameters of the CPW lines are a homogenous signal strip with a width of 50 μm and 25 μm gap with 5 μm metal thickness, assuming a conductivity of $\kappa = 3.52 \cdot 10^7 \text{ S/m}$. The material is alumina Al_2O_3 ($\epsilon_r = 9.7$, $\tan \delta = 0.000125$, thickness 625 μm). The wafer has a rectangular shape and is placed on a thick ceramic chuck ($\epsilon_r = 6.0$, $\tan \delta = 0.02$, thickness 2000 μm), which emulates a lower open boundary condition in the direction of the substrate thickness. What is varied is the ground (GND) width of the CPWs, choosing a value of 50 μm , which is referred to as "narrow" in the following, a GND width of 270 μm ("standard"), and a larger GND width of 650 μm ("wide").

Table 1: Dimensions of the investigated wafer

Parameter	Value
Substrate thickness h	625 μm
Signal width w	50 μm
Gap g	25 μm
Metal thickness t	5 μm
Conductivity κ	$3.52 \cdot 10^7 \text{ S/m}$
Relative permittivity ϵ_r	9.7

3.1.1 Influence of CPW ground width

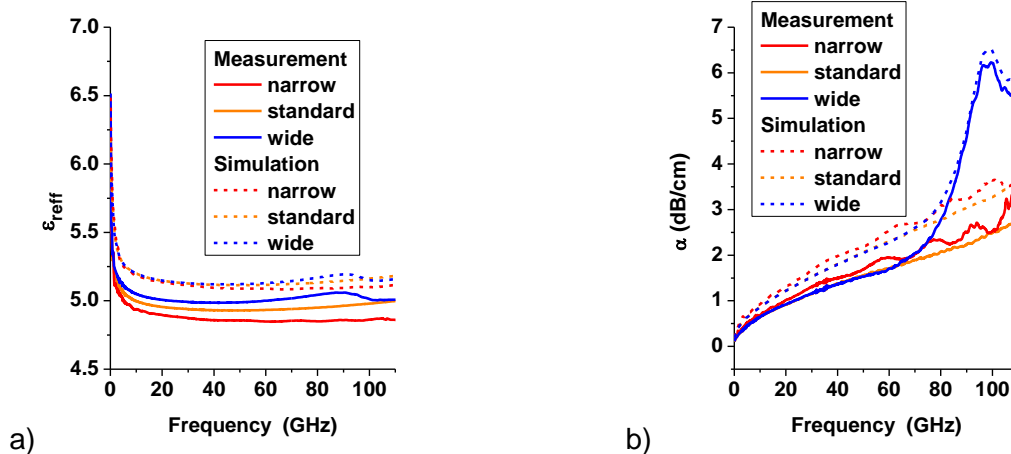


Fig. 9: Propagation constants for CPWs with narrow, standard, and wide ground width.

In order to include all the effects of a realistic measurement setup in the simulation, the complete wafer with its environment is included in the simulation. For excitation, a detailed probe model is applied. The measured and simulated effective permittivity and attenuation up to the W band are shown in Fig. 9 a) and Fig. 9 b), respectively.

One can observe a relatively good agreement between simulation and measurements (less than 5% deviation for effective permittivity). Moreover, it is important to note that the measured and simulated curves exhibit the same peculiarities at the same frequencies. While the CPW with standard ground width shows "typical" CPW characteristics for effective permittivity and attenuation, the CPWs with wide and

narrow grounds reveal some discrepancies. The CPW with wide ground width shows the expected behavior up to 80 GHz, but beyond an increase is observed which then turns into a peak at 100 GHz, both in effective permittivity and attenuation. The CPW with narrow ground, on the other hand, yields a well-behaved characteristic in effective permittivity but strange (unwanted) ripples in the attenuation. The reason for the ripples in the attenuation of the narrow CPW can be attributed to the special pad structure which differs from the other CPW types.

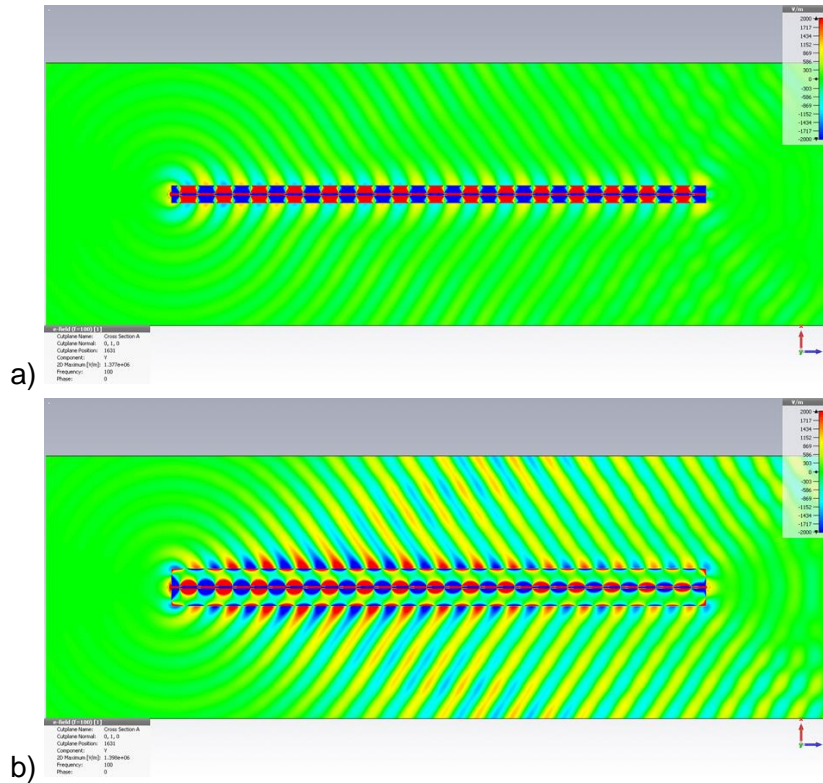


Fig. 10: Vertical electric field for the CPW with standard a) and wide ground b) width (CPW with simplified excitation on infinite chuck material with $\epsilon_r = 9.7$).

In order to understand the dip behavior in the attenuation constant for the CPW with wide ground width, the vertical electric fields for the standard and wide ground are shown in Fig. 10. The fields for the CPW with standard ground width exhibit the typical field distribution of a CPW mode whereas the fields for the CPW with wide ground width show a pattern with much stronger radiated fields.

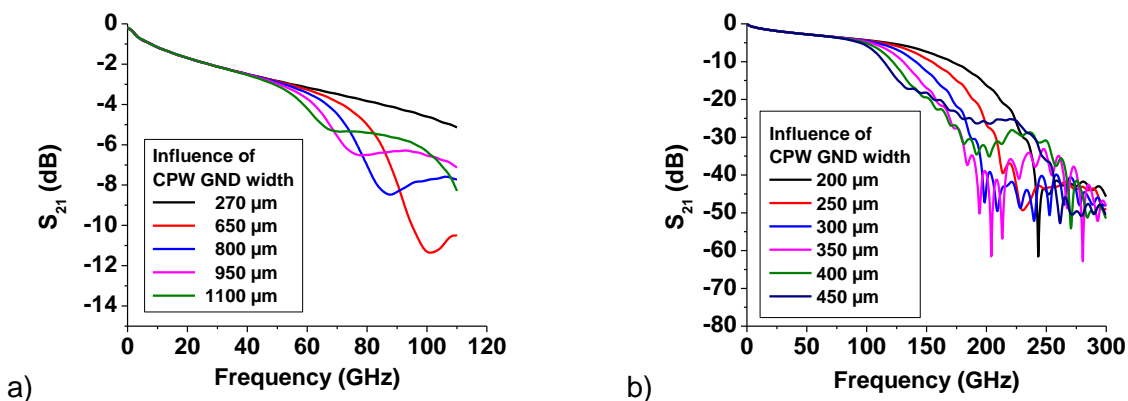


Fig. 11: Transmission coefficients S_{21} when varying CPW ground width on ceramic chuck: a) up to the frequency range 110 GHz; b) extension of the frequency range until 300 GHz.

In order to determine the dependency of the dip frequency on ground width, additional simulations varying the ground width were performed. Comparing these results (Fig. 11), one can observe that the dip (or peak) behavior is determined by the size of the ground width. The larger the CPW ground width, the lower is the frequency where the dip occurs.

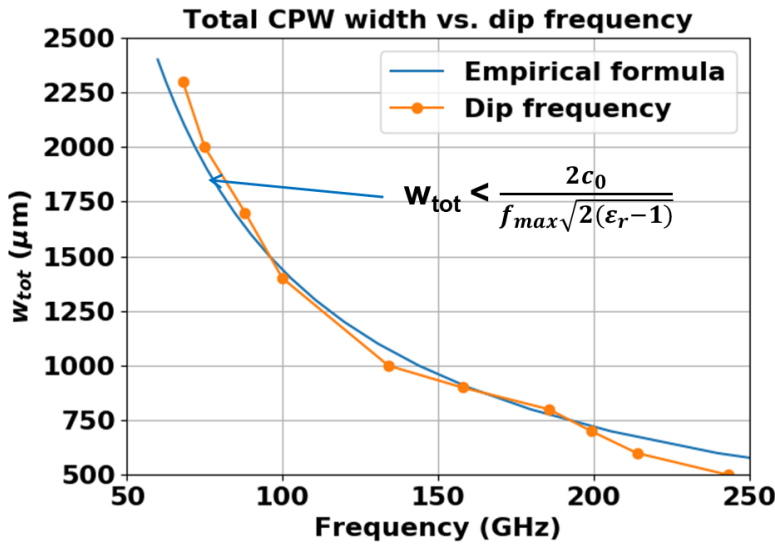


Fig. 12: Total CPW width vs. dip frequency in comparison to an empirical formula from [8].

Fig. 12 plots the total CPW width vs. dip frequency in comparison to an empirical formula **from [8]**.

$$w_{tot} < \frac{2c_0}{f_{max}\sqrt{2(\epsilon_r - 1)}}$$

As can be seen the empirical formula described the behavior of the dip frequency surprisingly well.

3.1.2 Impact of ground-to-ground spacing

In order to distinguish the impact of the ground-to-ground spacing from effects of the total CPW width, which represents the ground-to-ground spacing plus double the ground width, this section focuses on the investigation of the ground-to-ground spacing. A constant total CPW width of $w_{tot} = 1000 \mu\text{m}$ is assumed and only the ground-to-ground spacing is varied. To maintain the characteristic impedance of 50Ω , the relation w/d is kept constant. The signal width is varied between $w = 25, 50, 75 \mu\text{m}$ and the CPW gap between $s = 12.5, 25.0, 37.5 \mu\text{m}$, which results in a ground-to-ground spacing of $50, 100$ and $150 \mu\text{m}$, respectively.

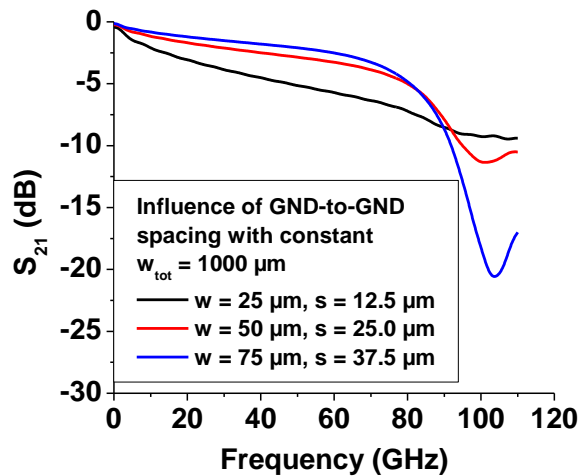


Fig. 13: Transmission coefficients S_{21} against frequency when varying ground-to-ground spacing and keeping total width constant.

Fig. 13 suggests that the position of the dip frequency does not change significantly for different ground-to-ground spacing. Only the strength of the dip behavior varies.

Guideline #4

The influence of CPW ground width and of ground-to-ground spacing, are contributing to parasitic effects in the calibrated results, in this case a dip in S-parameters at a certain frequency.

Total CPW **width** determines the frequency where this dip occurs, and **ground-to-ground spacing** influences the strength of the dip behavior.

Thus, the best way to mitigate the impact of this dip is to keep the total CPW width smaller than the formula given in [8], which requires a tradeoff between the CPW total width, the used material and the upper frequency limit f_{max} .

3.2 Probe topology

Another source of deviations can be the use of different probe types. The influence of the probe should be considered in combination with the respective environment close to the tips when contacting the wafer. The impact of probe geometries is demonstrated in the following subsections.

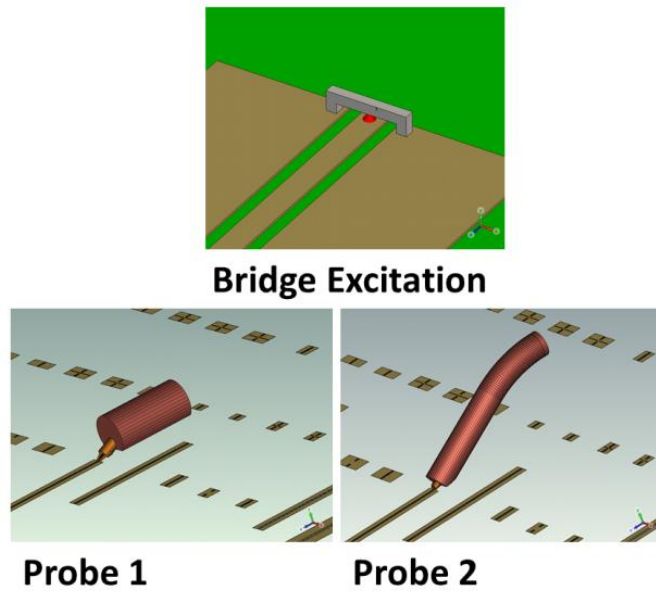
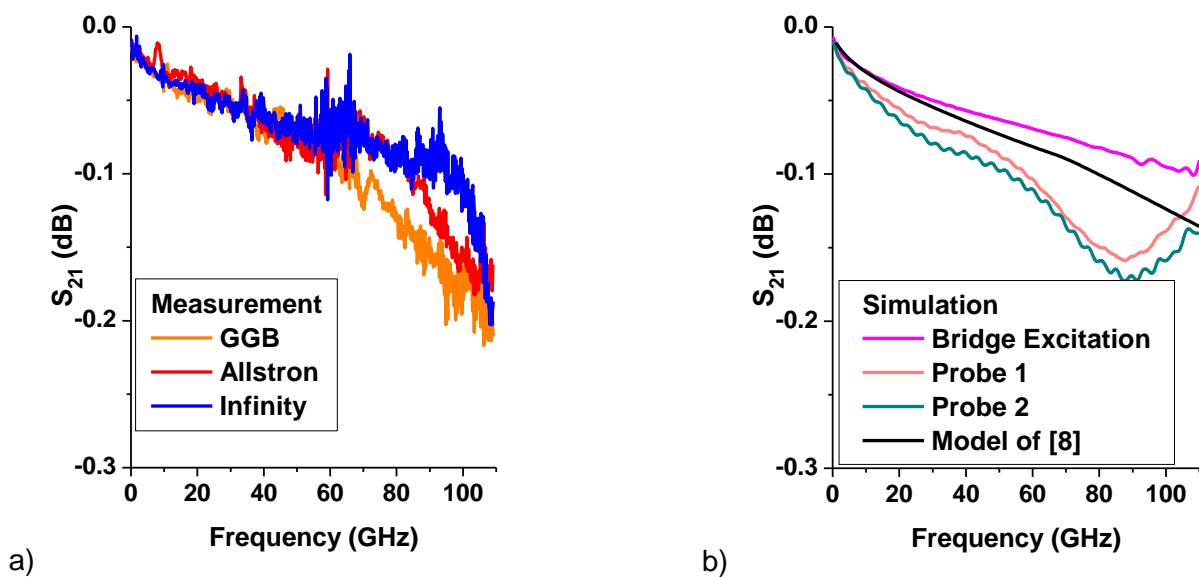
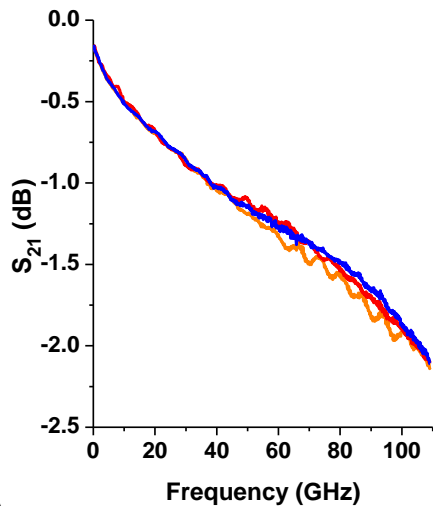


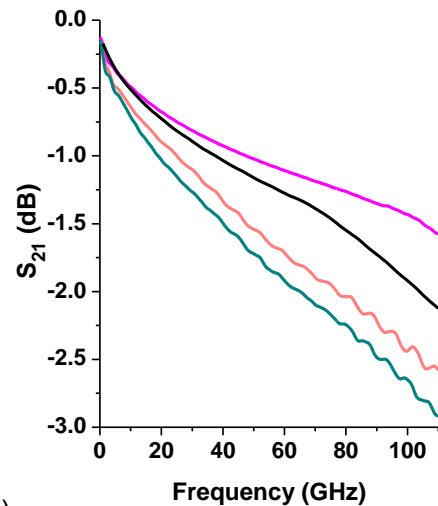
Fig. 14: Different excitation structures used in the EM simulations.

In order to investigate the influence of the probes, we performed additional measurements and simulations for the CPW with standard ground width, using two other probe types from different manufacturers. In the simulation, we include the complete wafer and excite the DUT with three different structures, a simplified bridge model similar to [13] and two probe versions, *Probe 1* and *Probe 2* (see Fig. 14). Then, we compare the results with the analytical model of [8] which yields the transmission line parameters directly without deembedding. Probe 1 stands for a geometry with relatively long needles, a thick absorber enclosing the coaxial feeding line, and a straight coaxial extension, oriented in parallel to the wafer. In contrast, Probe 2 has a steeper slope of the coaxial extension. This emulates the case where the probe is not oriented parallel to the wafer.





c)

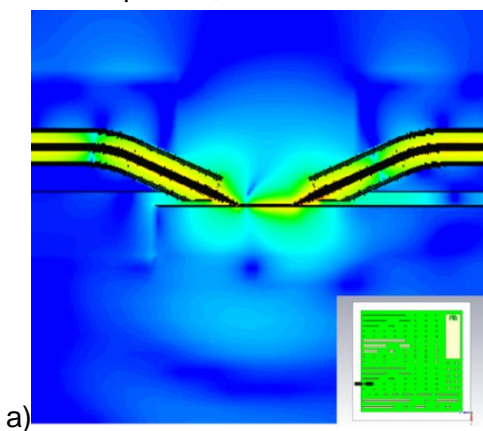


d)

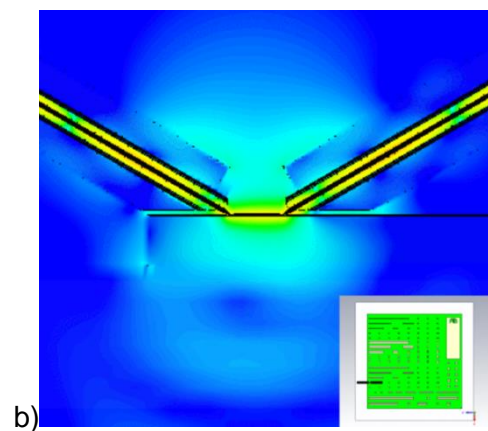
Fig. 15: Calibrated results for the magnitude of S_{21} for a CPW of 500 μm (a and b) and 7400 μm (c and d) length; left: Measurements with different probes; right: Simulations with different excitations compared to model of [8] (legend shown in top graphs).

Although the deviations between the probes do not appear to be very significant, particularly for the short line, Fig. 15 reveals an interesting behavior. The same CPW measured with different probes shows different results, with deviations up to 0.2 dB for the long line (Fig. 15 c). The focus of our investigation is not primarily to determine the maximum deviation. It is to explain how the properties of the probe can change the resulting calibrated data. For a short CPW line of 500 μm length, one normally assumes that the curve behavior would follow a smooth function with a slight increase at higher frequencies comparable to the model of [8] in Fig. 15 (b). However, the measured calibrated results (Fig. 15 a and c) as well as the simulated results with Probes 1 and 2 exhibit a wave-like behavior which does not appear at all in the model of [8] or the simulation with bridge excitation (least parasitics). The simulation with probe excitation, on the other hand, reveals the various parasitics of the probe excitation, i.e., coupling from probe to substrate modes, radiation, and fringing fields between the probe and other structures.

This means that the reasons for the unphysical curve behavior for the propagation constants can be attributed to the probes, in combination with the calibration process.



a)



b)

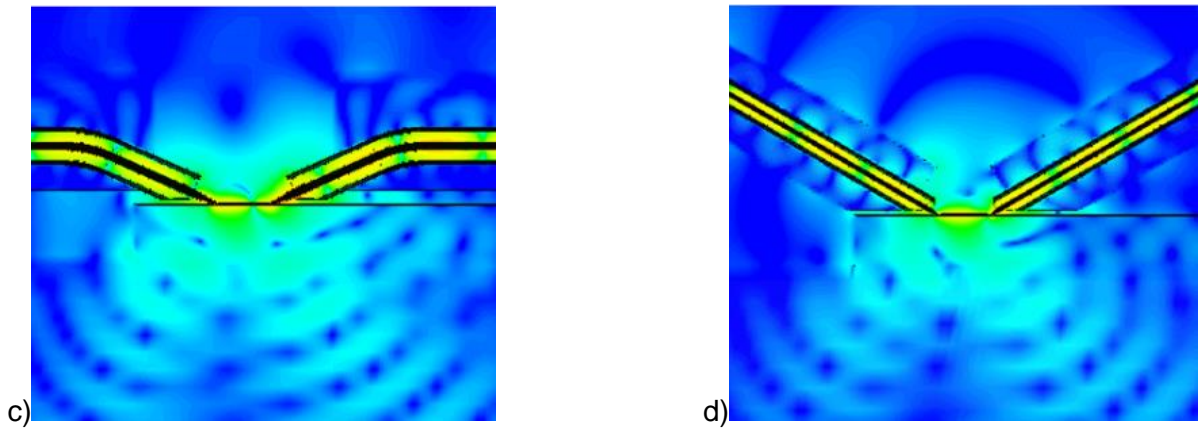


Fig. 16: Field plots: magnitude of the electric field for a 700 μm long CPW excited with different probes; left (a and c): probe 1; right (b and d): probe 2, top: at 50 GHz; bottom: at 100 GHz.

The field plots shown in Fig. 16 illustrate the influence of the probe construction (note that the left-hand probe is located at the wafer edge). Fig. 16 shows that, depending on the geometry of the probe needles and the absorber construction, the fields around the probe transition are distributed differently. The electric fields within the air region below the left-hand probes differ from the fields below the right-hand side probes. Also, the fields in the close vicinity of the CPW and the probe tips differ, as do the fringing fields between the probes, which are clearly higher as in the case of the bridge excitation.

3.3 Chuck topology

Both phenomena (radiation depending on the cross-section dimensions of the CPW as well as the impact of the probe type) are related to the generation and propagation of substrate modes. The parasitic effects due to the propagation of the substrate mode cannot be completely avoided for this layered system. But they are strongly dependent on the permittivities of the chuck material and the wafer.

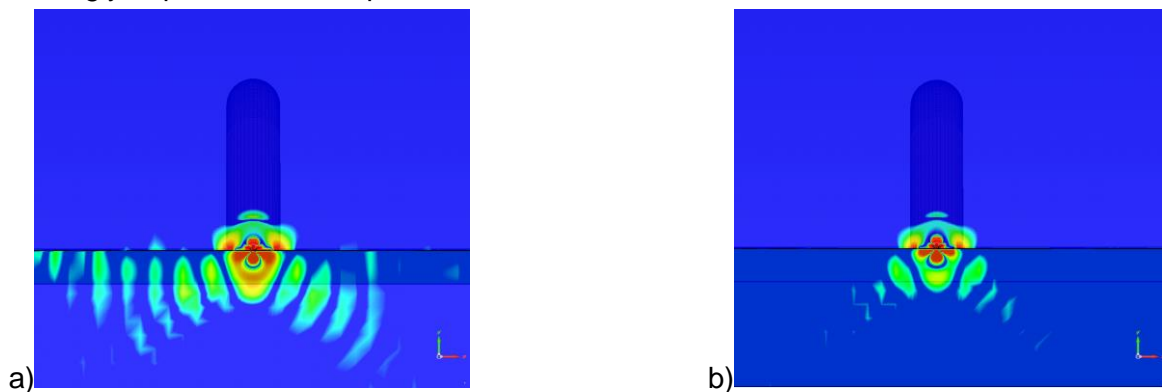


Fig. 17: Vertical electric field component excited with probe 2 at 100 GHz (cross section); a): on ceramic chuck $\epsilon_{r,\text{chuck}} = 6.0$; b): on chuck with same permittivity as the wafer, i.e., $\epsilon_{r,\text{chuck}} = 9.7$. Due to finite discretization cells used in simulation only a moderate resolution of the field pattern can be displayed.

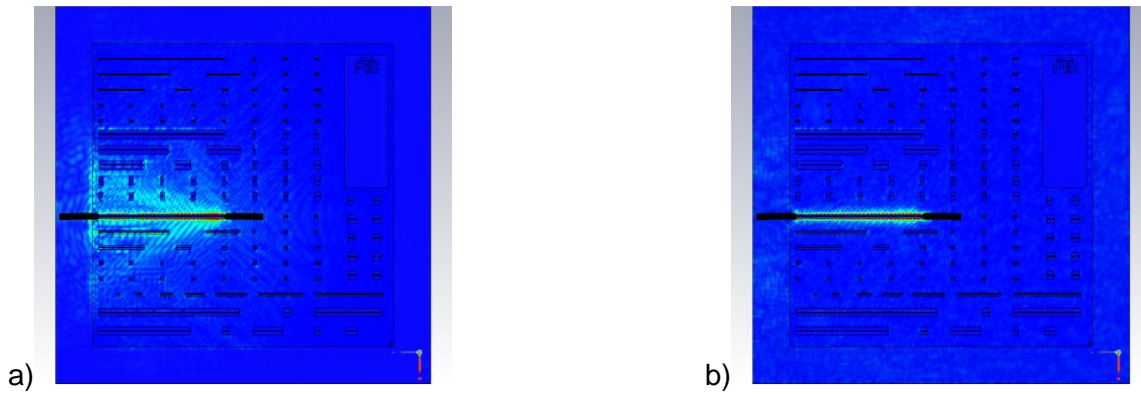


Fig. 18: Field plots: magnitude of the electric field at 100 GHz (top view) excited with probe 2 for nominal CPW ground width; a): on ceramic chuck $\epsilon_{r,\text{chuck}} = 6.0$; b): on chuck with same permittivity as the wafer, i.e., $\epsilon_{r,\text{chuck}} = 9.7$.

E.g., if the wafer is placed on a chuck with same permittivity as the wafer, the substrate mode vanishes because then wafer and chuck form a homogeneous medium, which does not support a surface wave mode any more. Fig. 17 and Fig. 18 support these statements, comparing the vertical electric field component for the CPW line (20400 μm) on different chuck materials. If the chuck permittivity is lower than that of the wafer (here, a ceramic chuck with $\epsilon_{r,\text{chuck}} = 6$ is used), one observes a superposition of radiation effects and propagation of a substrate mode which is generated at the probe tips due to the layered structure. Accordingly, in Fig. 18 (a), the electric fields spread over the whole wafer and are reflected back at all discontinuities and edges.

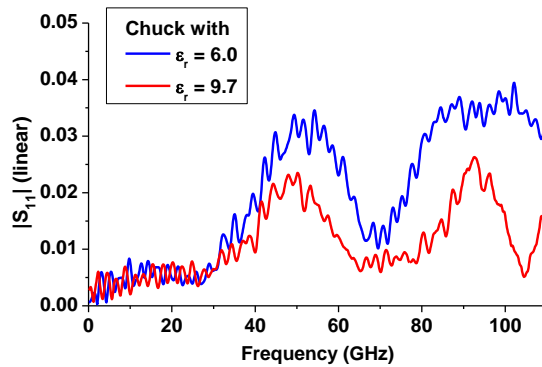


Fig. 19: Calibrated simulation results of the magnitude of S_{11} for a 20400 μm long CPW on different chuck materials.

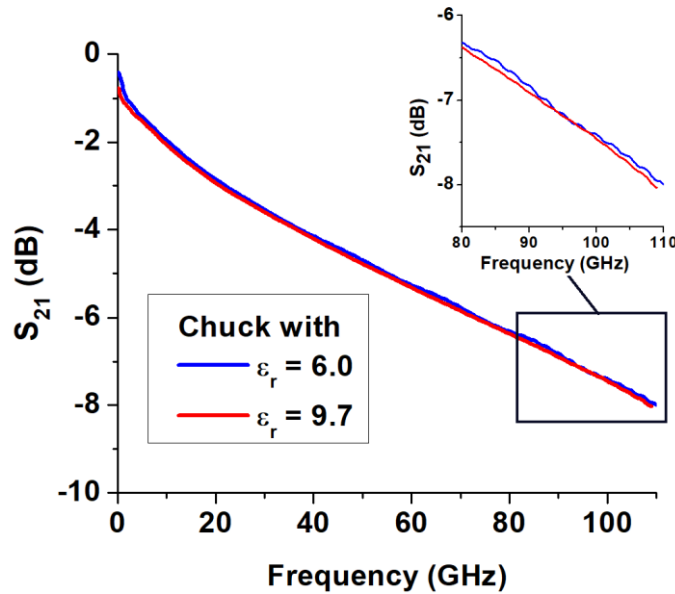


Fig. 20: Calibrated simulation results of the magnitude of S_{21} for a 20400 μm long CPW on different chuck materials.

If the chuck has the same permittivity as the wafer (Fig. 17 and Fig. 18 b), the substrate modes are suppressed. Therefore, the lateral spreading fields do not appear anymore and also the reflection coefficient (see Fig. 19) exhibits lower values. This in turn leads to fewer ripples and a smoother curve behavior in the transmission coefficient S_{21} (see Fig. 20).

Guideline #5

Using for the chuck a material which has a permittivity value similar to the calibration substrate reduces the effects which contribute to the degradation of the accuracy of CPW mTRL calibrations.

Further investigations have shown that this is true also for a chuck material with a permittivity larger than that of the wafer, because such a layered structure does not support surface waves either.

3.4 Design guidelines related to the probe construction for coplanar waveguides

In order to clarify the impact of probes, this section will focus more on effects related to the probe and the interaction with its vicinity. In general, there are essentially four reasons detectable – the probe, the line structures, the circuit design (density, pattern) and the wafer structure (also chuck) and material. Many effects are related to the probe. Its size and shape, the GSG needle configuration (length, distance, opening of the coaxial line), the probe slant backwards to the probe head and the absorber material contribute to the fringing fields and thus generate modes. In order to simplify the structures but keep the effects valid we designed artificial probes. For the mTRL calibration we used line lengths of 550 μm (thru), 667 μm , 900 μm , 1600 μm , 2685 μm , 3700 μm , 7115 μm and 10000 μm as well as an open and short with 800 μm access line length at a total length of 3700 μm build upon GaAs ($\epsilon_r = 12.9$) with open boundary at the bottom side. With this assumption, a semi-infinite half space is emulated.

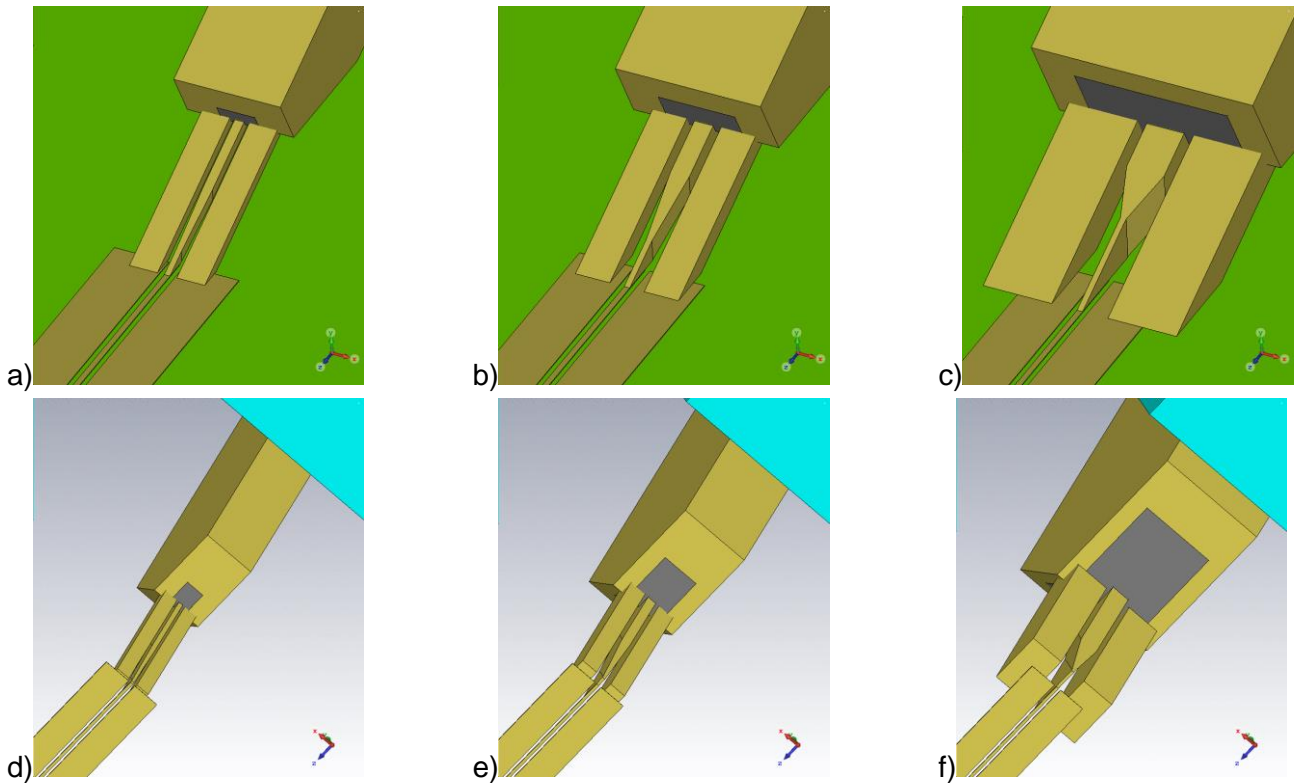


Fig. 21: The simplified probe systems with probes 1, 2 and 3 with the width and coaxial opening scaled from a to f. Upper row: Top view. Lower row: Bottom side without substrate.

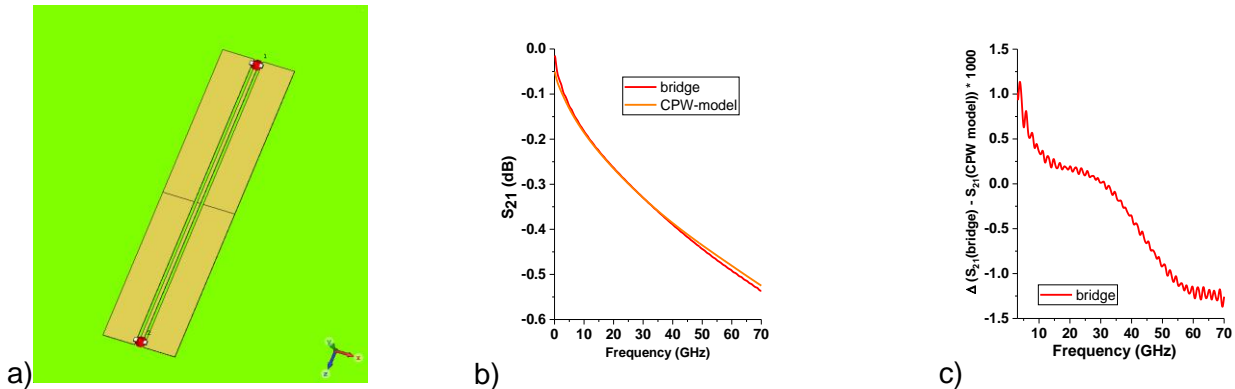


Fig. 22: A set of calibration lines excited with lumped ports placed in artificial bridges at the position of the probes. a): Line 3. b): Transmission S_{21} . c): Difference of S_{21} compared to the CPW model of [8].

In order to allow a basic simulation for the “true” performance of the CPW properties, a lumped bridge excitation is used. All the calibration structures were simulated and this data was then processed with the mTRL calibration algorithm. The extracted results are compared to the analytical CPW model [8]. Fig. 22 shows that the calibrated data of the bridge model coincide with the results of the analytical CPW model very well. Therefore, one can state that the bridge model can serve as a reliable reference for comparison.

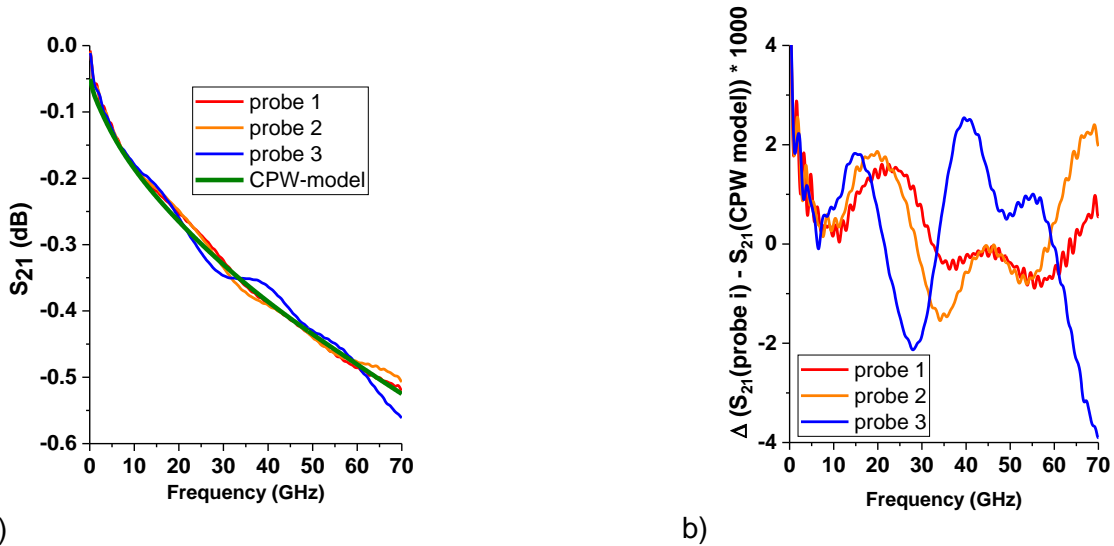


Fig. 23: The calibrated results of line 3 (1600 μm) for all 3 probes. a): Transmission S_{21} . b): Difference of S_{21} to the CPW model of [8].

Fig. 23 indicates that though the calibration process should deduct all effects of the probe and its environment leaving only the S-parameter of the measured DUT the curves show that the probe size (and shape) still generates deviations. The difference of the linear S_{21} to the CPW model of [8] is shown in Fig. 23 b. The maximum deviation is approximately 0.4% and occurs with probe 3.

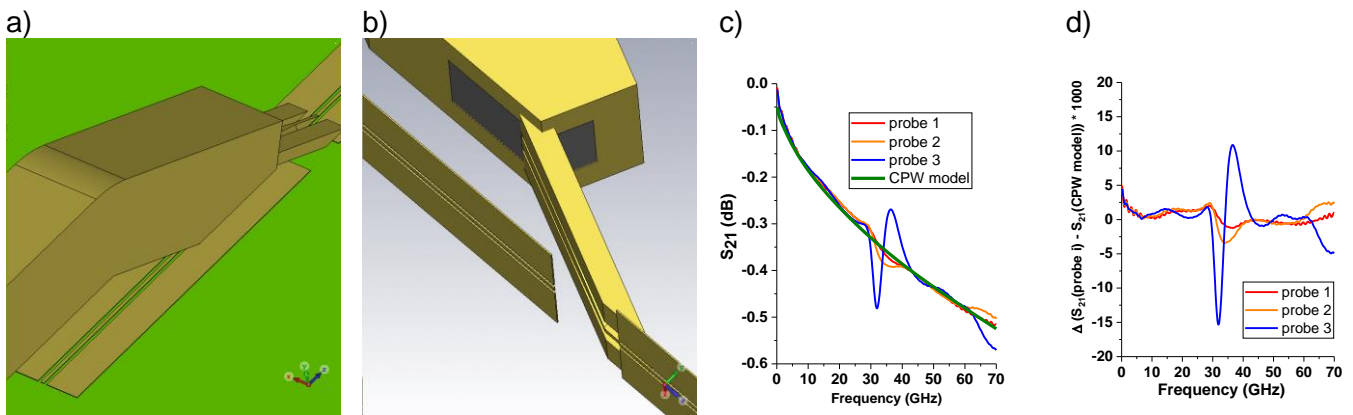


Fig. 24: (a and b) Probe 2 with in-line neighbor (length = 1.66 mm, distance to DUT = 200 μm). The calibrated results of line 3 (1600 μm) for all 3 probes; (c) transmission S_{21} and (d) difference of S_{21} to the CPW model of [8].

In order to include the probe interaction with its vicinity, a neighboring structure is added in in-line direction to the DUT. Fig. 24 c and d show the comparison of the calibrated results for the configuration with a DUT and a neighboring structure excited with the three different probes. At the first glance, one can observe a dip or resonance behavior in all the curves due to the interaction with the in-line neighboring structure. It is important to note that the strength of the dip behavior differs depending on the size of the probes. Probe 3 with its large dimensions shows the most emphasized dip behavior which yields a maximum deviation of 1.5 %. Therefore, the influence of metal configurations in the vicinity of the probe needle region can have strong effect on the DUT measurement. One needs to separate these investigations into two cases, metal inside or outside the probe shadow, which is referred to as the area below the probes that would be shadowed if the probe would be illuminated from the top. Further

investigations concerning the influence of in-line and side-way neighboring structures have been performed.

Guideline #6

The results reveal that one should keep sensitive regions of the probe shadow free of structures to avoid probe coupling to neighboring structures, as shown in Fig. 25 (investigations performed up to 70 GHz).

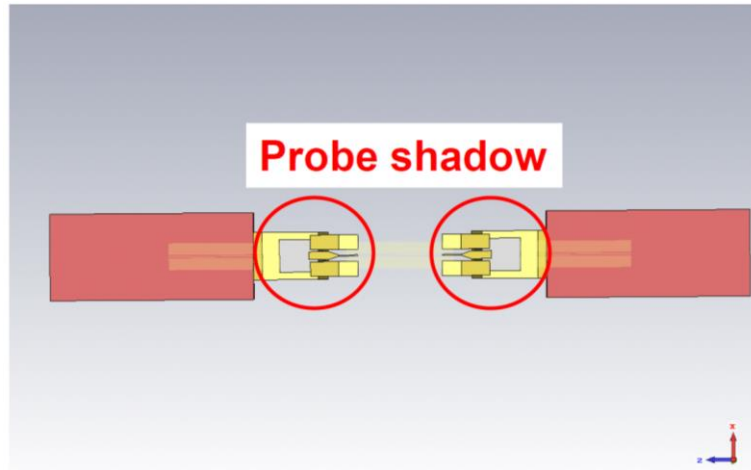


Fig. 25: Design recommendations related to the probe construction.

3.5 Thin-film Microstrip lines (TFMSL)

While the situation with coplanar waveguides has been discussed in the previous sections, the purpose of this section is to add the respective results for thin-film microstrip lines. In order to perform the investigations, wafers with different layouts were designed and fabricated. What is studied here is the impact of positioning of the calibration structures and of the probe on the calibrated results of the different DUTs. Therefore, two sets of calibration lines on two diced reticles are used. Both sets were fabricated on the same wafer. The process comprises a thin-film multilayer stack which is realized on top of a 500 μm thick Borofloat substrate.

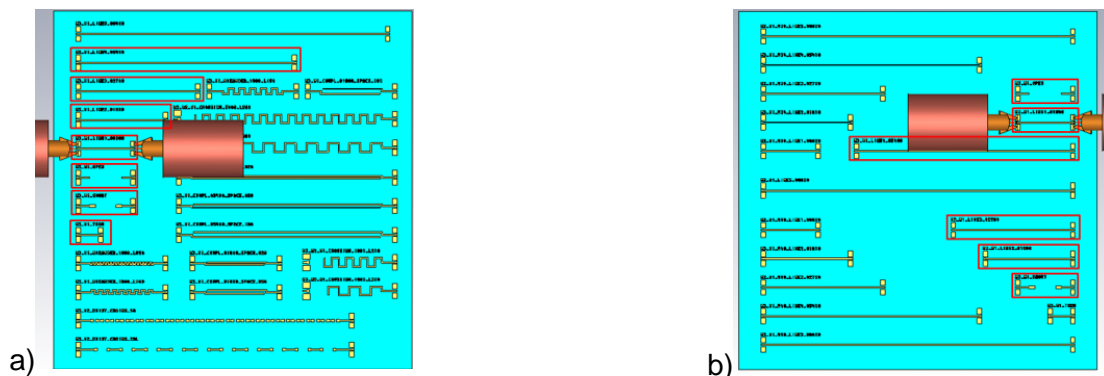




Fig. 26: a): Layout of reticle 1 (c) : photograph of a zoomed part of reticle 1); b): Layout of reticle 2 d): zoomed region around the right probe tip.

The ground layer is buried in the 18 μm thick Benzocyclobutene (BCB) layer stack, the signal strip metallization level (with a thickness $t = 5 \mu\text{m}$) is located on top of the BCB. An intermediate metal layer level can be added. This process was developed at FhG IZM as motherboard for microwave modules but can be treated as an example for other thin-film wafer topologies as well. The measurements of the calibration structures and DUTs are performed on a chuck with a 1 cm thick ceramic support. Fig. 26 top shows the layouts of the two calibration sets. Each includes a complete set of line elements, consisting of 4 thin-film microstrip (MS) lines (signal width $w = 37 \mu\text{m}$) of different lengths ($l = 900, 1800, 2700$ and $5400 \mu\text{m}$), as well as an open and a short structure as reflect standards. Loads were not implemented because resistors were not available on this specific wafer run (in general, the process includes resistors). One thru line failed (reticle 2) so that for all possible combinations only one thru line could be used. From the structures (see Fig. 26), we obtained two calibration sets: Cal 1, by using the set on reticle 1, and Cal 2, by using the set on reticle 2 (here with the thru line of reticle 1).

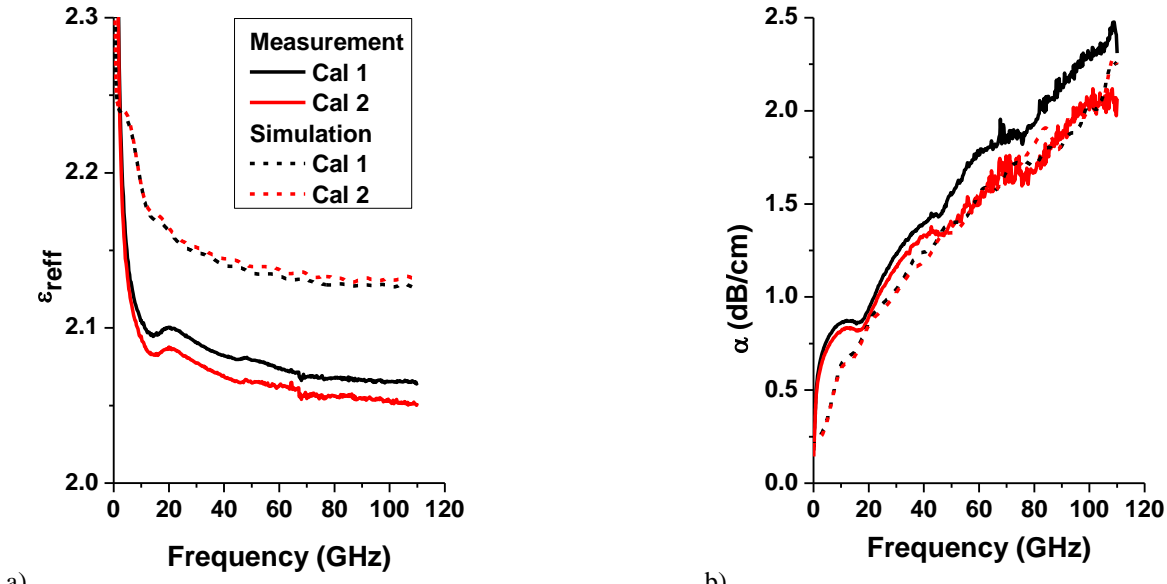


Fig. 27: Effective permittivity (a) and attenuation (b) of measured and simulated calibration sets Cal 1 and Cal 2.

In reticle 1 (see Fig. 26 a), all the calibration structures are located on the left-hand side of the reticle, next to the edges of the reticle whereas in reticle 2 (Fig. 26 b) the calibration structures are placed on the right-hand side of the reticle. In the labeling of the probe and the S-parameter set, the index 1 always denotes the left and index 2 the right-hand side. Also, all elements are placed in a different environment regarding the neighboring structures. After measuring and simulating all the calibration elements, the TRL calibration process was applied to the measured and simulated data of both calibration sets 1 and 2.

The first results of the TRL calibration are the line properties which are plotted in Fig. 27. Comparing the effective permittivity and the attenuation constant one observes already slight differences between the two sets for both measured and simulated results. The deviation of the measured data at 40 GHz in ϵ_{reff} is about 4% and in α about 12%. This is partly clouded by the deviations between simulation and measurements, which are probably due to the fact that the modeled probe does not map the real probe geometry completely and the limited knowledge of the material properties of the wafer.

The question is whether and how these admittedly relatively small deviations between the two calibration sets will influence the calibration of a DUT. Therefore, the impact when changing between the calibration sets (Cal 1 and Cal 2) on two selected DUTs will be investigated. These DUTs are a daisy chain (DUT1) and a coupled line structure (DUT2).

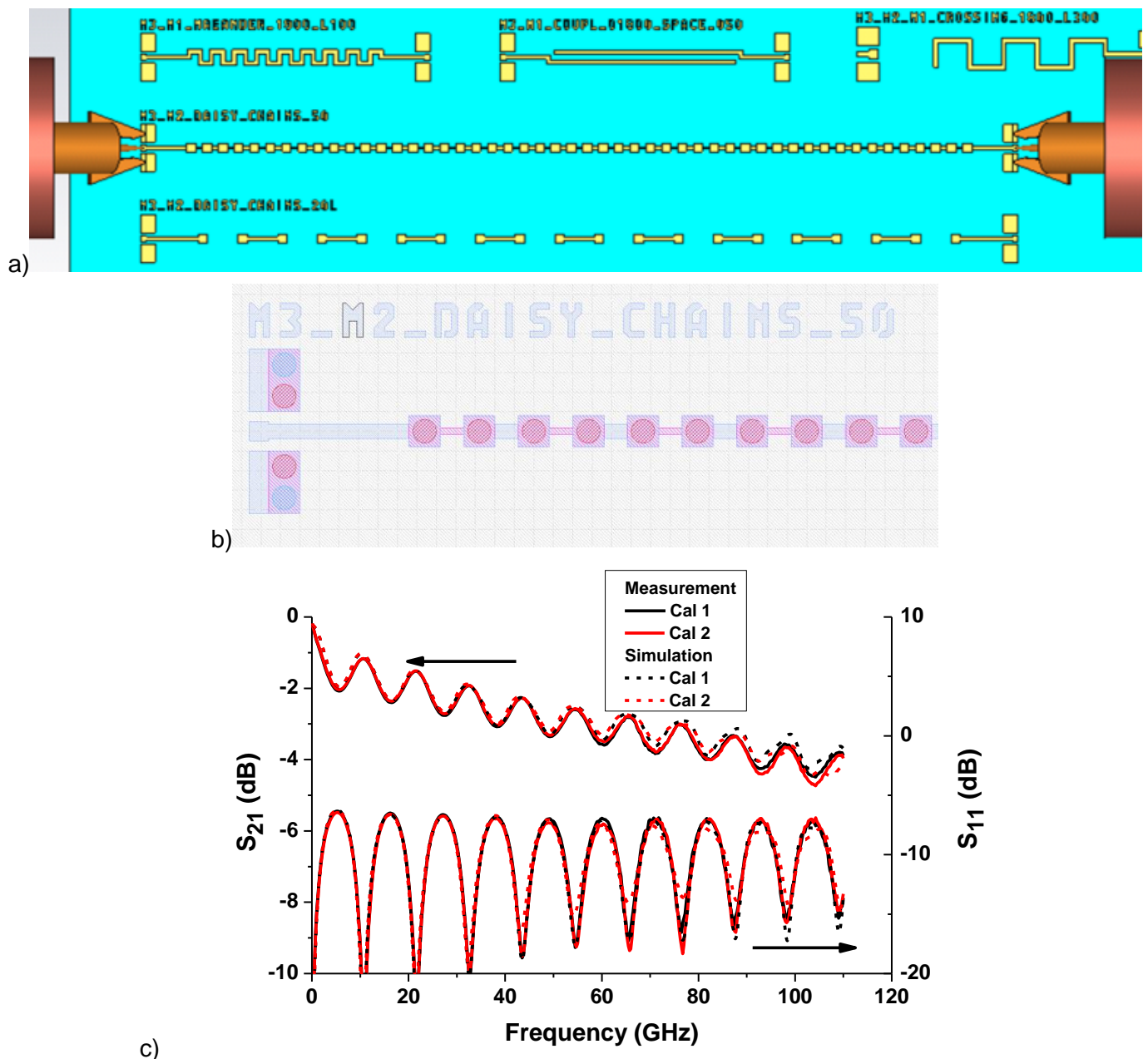


Fig. 28: DUT 1 is a daisy-chain configuration using 50 via transitions, a): geometry for simulation, b): layout configuration, c): calibrated results of measurements and simulations using Cal 1 and 2.

DUT 1 (Fig. 28) is a daisy-chain configuration using 50 via transitions placed at the lower wafer side of the reticle (Fig. 1 a). It is surrounded by neighboring structures at the sides, such as meander line, couplers, and another daisy chain.

DUT 1 is an example of a structure with high transmission and low reflection. It has no in-line neighbors. The results after calibration are presented in Fig. 28. One finds good agreement between all 4 results (measured and simulated data for Cal 1 and 2). The deviations between the two calibration sets can be neglected. The differences in effective permittivity become apparent only in the upper frequency range and deviations in attenuation cannot be seen at all, due to the fact that all corrections by the calibration process relate to very short structures and thus the attenuation has minor influence. In general, we observe this low sensitivity to calibration impairments for all DUT types with low reflective properties like thru-lines, filters and daisy chain structures.

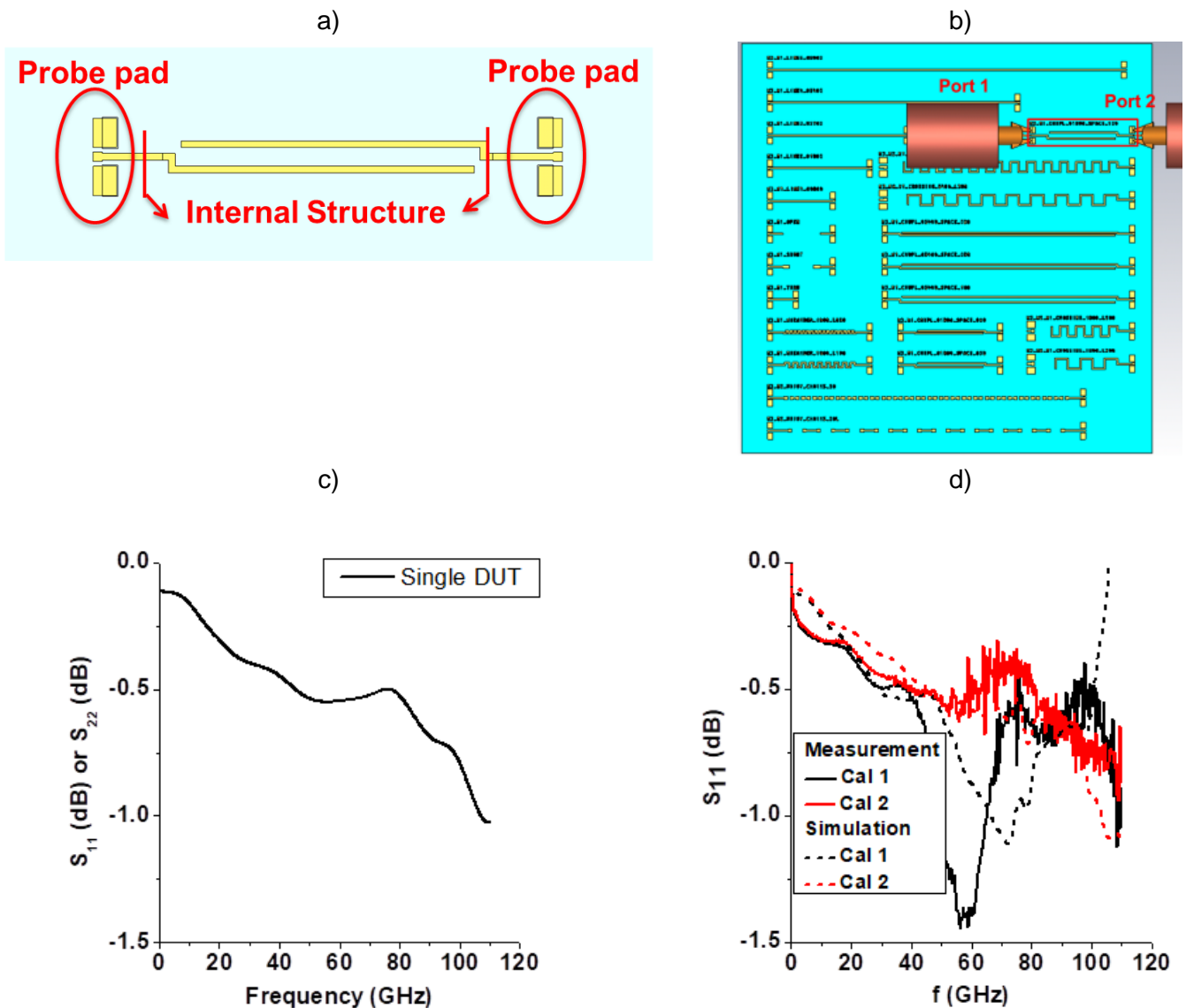
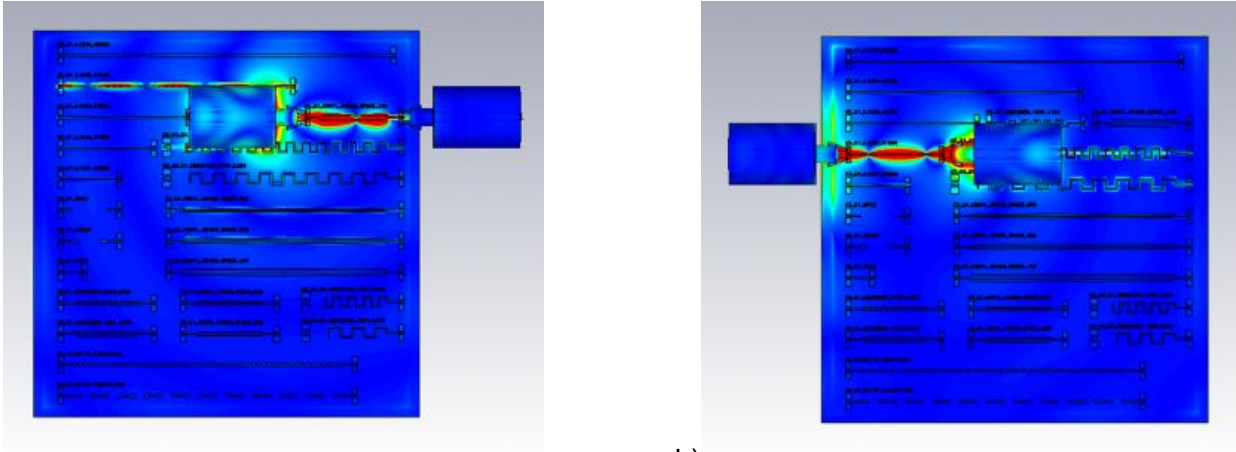


Fig. 29: DUT 2 is a coupled-line configuration with 1800 μm coupling length (a): DUT2 placed on a wafer (b); (c) : expected behavior of DUT2 and d): Measured behavior of DUT 2 compared to simulation.

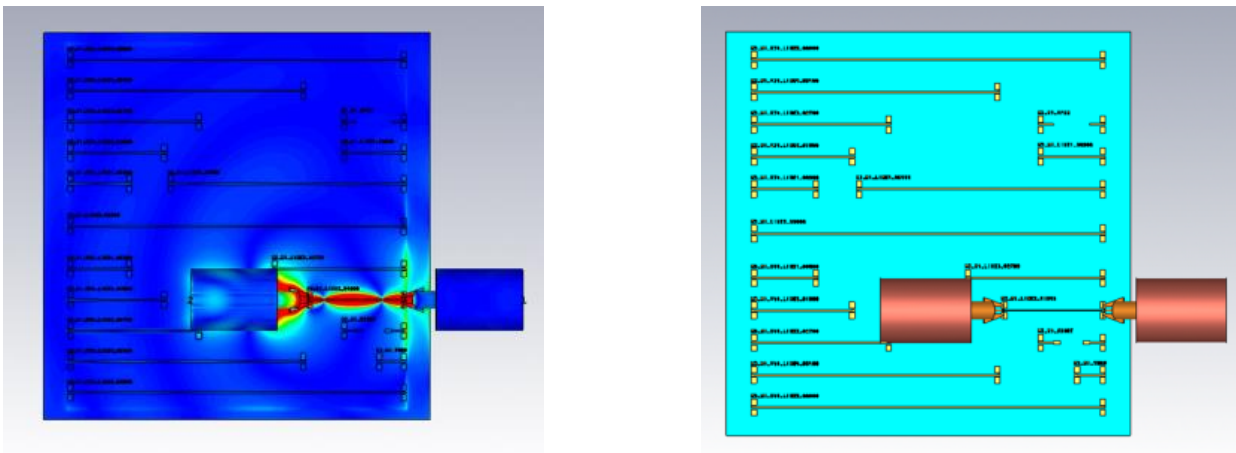
DUT 2 (Fig. 29 a) is a coupled-line configuration with two parallel strips in a distance of 100 μm and is placed on the right-hand side of reticle 1, with the right termination similar to the calibration elements on reticle 2 (see Fig. 29 d). It is placed next to a meander line and one of the calibration lines and has

another calibration line in longitudinal continuation on the left-hand side. It is a highly reflective element with low transmission. S_{11} in Fig. 29 right shows good agreement between measured and simulated data for Cal 2, but a much worse behavior for the Cal 1-based results with an unexpected dip around 60 GHz (the shift between measurement and simulation is due to the probe model). Using Cal 2 simulation and measurement, results agree well and are as expected. But, as for S_{11} , the results reveal distinct deviations when the calibration Cal 1 is applied to the raw data.

In order to clarify this unexpected behavior, we simulate the fields at 68.42 GHz for the DUT 2 as well as for line 2 in the two calibration sets.



a) b)
Fig. 30: Magnitude of electric field (i) around DUT 2 on reticle 1 for excitation of probe 1 (a), and (ii) around line 2 in reticle 1 for excitation of probe 1 (b).



a) b)
Fig. 31: Magnitude of electric field around line 2 in reticle 2 for excitation of probe 1 (a), and corresponding measurement set-up (b).

The field plots in Fig. 30 and Fig. 31 illustrate the magnitude of the electric field around the DUT and the line element when exciting with probe 1 (a). It is obvious from the field plots that the field distribution at line 2 for the two reticles differs significantly (Fig. 30 right, Fig. 31 a).

More precisely, there is coupling into the neighboring structures for both DUT 2 and line 2 (Fig. 30), which does not occur at line 2 in Fig. 31 with no in-line neighbor.

The field distribution around the excited left probe of DUT 2 (Fig. 30 a) differs from the field distribution around the excited left probe of line 2 on reticle 2 (Fig. 30 a). The different properties are linked to the neighboring structures. All right-hand terminations of the calibration lines of Cal 2 are located at the right-hand edge of the substrate and the left terminations of the lines of Cal 2 are positioned in the interior

region away from the edge. The arrangement of the calibration lines of Cal 1 is opposite: The left-hand terminations are close to the substrate edge, while the right-hand ones are located in the interior part. Thus, the fields excited by the probe at the right-hand terminations of the lines in Cal 2 are similar to the fields excited by the probe at the left-hand side of the lines in Cal 1. Therefore, the calibration algorithm will generate different results for the error matrices of the ports when using Cal 1 and Cal 2, respectively, and thus accuracy degrades.

3.6 Design guidelines related for thin-film microstrips

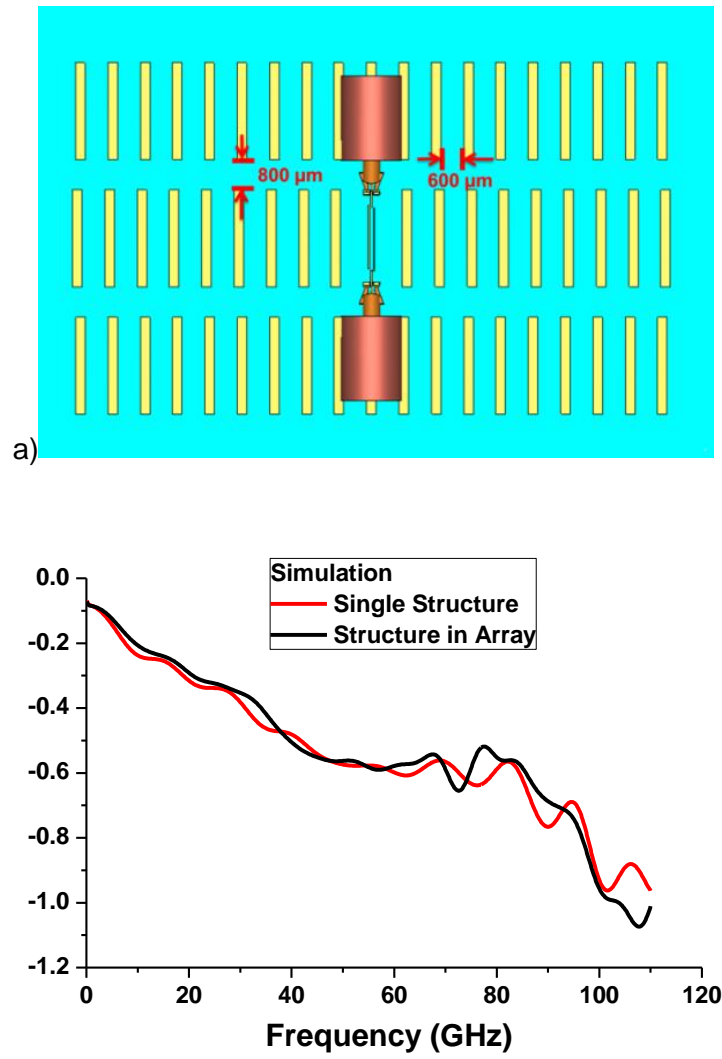


Fig. 32: Matrix configuration of DUT and neighboring lines (a); simulation results of the matrix configuration in comparison to a single stand-alone DUT (b).

From the results above and further investigations on similar structures we can derive design rules that help to reduce unintended side effects like coupling to neighbors or wafer/reticle edges. Fig. 32 b illustrates a solution with sufficiently good properties, i.e., sufficient distance between the prober and the structures adjacent to the DUT. A value of 800 μm was chosen here.

Guideline #7

Basic layout conditions that should be fulfilled (extracted from the case of thin-film MS to substrate separation of 18 μm thick).

- (1) Place the calibration elements at sufficient distance

(2) Do not place structures within the probe shadow region below the probe (Fig. 33 illustrates this). In contrast to the CPW case, the parasitic effects in a TFMSL environment are not related to substrate modes and crosstalk between structures, but only to coupling from the probe to the surrounding structures by fringing fields.

For thin-film microstrip lines as was the case for coplanar waveguides, one needs to keep the region of the probe shadow free of structures to avoid accuracy degradation.

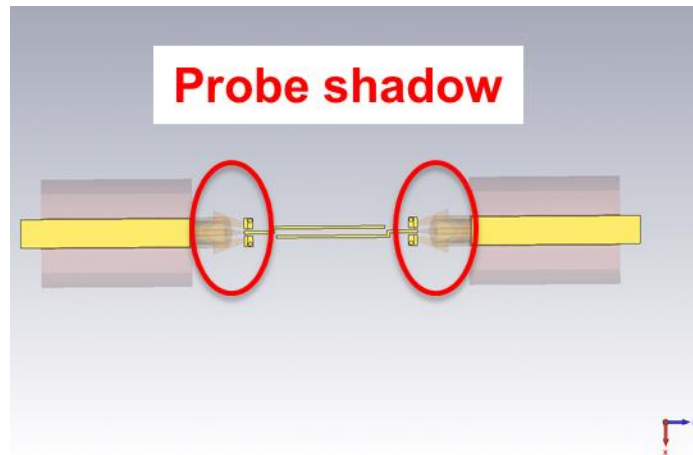


Fig. 33: Defining the critical area around the probes, referred to a probe shadow.

4. Example of custom designed TRL kit

In this section to provide a practical example of a custom calibration kit design a full set of standards is designed and fabricated to perform a TRL calibration in the back-end-of-line (BEOL) of the IHP 130 nm SiGe BiCMOS process.

Uniform grounded CPW lines have been considered following the points described in Section 1 of this guide. The fabricated chip microphotograph of the TRL kit is shown in Fig. 34 (i.e., thru, reflect and line, respectively a, b and c).

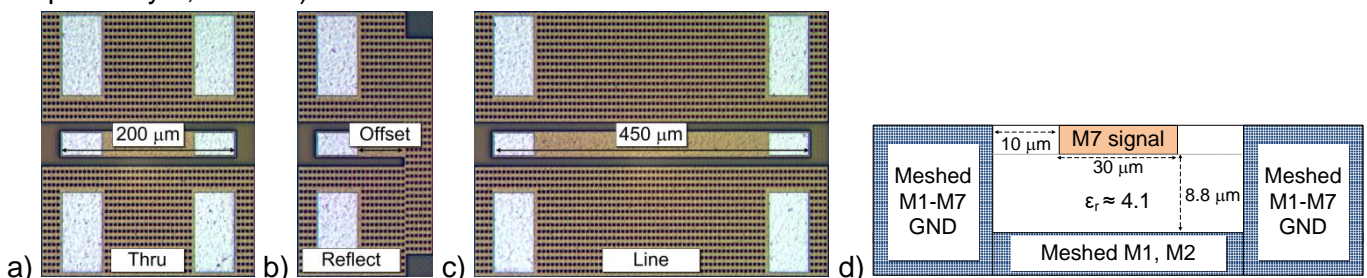


Fig. 34: CPW calibration artefact realized on IHP SiGe 130 nm BiCMOS technology. (a) Microphotograph of the thru line, (b) of the reflect standard and (c) of the transmission line employed for the WR05 calibration kit. (d) Cross section sketch of the CPW line.

The lines are implemented as grounded CPW (CPWG), to reduce losses in the (semi) conductive substrate. All the structures employ aluminium pads, i.e., signal pad $30 \times 50 \mu\text{m}^2$ and larger grounds pads to allow different probe pitch to be used on the same structure (i.e., $75 \mu\text{m}$ and $100 \mu\text{m}$). The thru line is a $200 \mu\text{m}$ long uniform coplanar waveguide (Fig. 34a).

The calibration kit reflects are realized by two symmetric offset shorts (Fig. 34b), with an offset equal to half the thru length. This minimizes the distance between the centre of the thru and the location of the short, allowing to fix the sign of the square root solution in the TRL calibration (i.e., +/- open/short) for the entire calibration band. Note that when an electrical length of $\lambda/8$ is present the sign needs to be changed to enforce phase continuity as shown in Fig. 35, where the wanted behaviour is shown in red while the achieved one in blue. The error presented in the case where an electrical length is present between the centre of the thru and the short plane (Fig. 35 a) can be corrected using offset shorts as shown in Fig. 35 c.

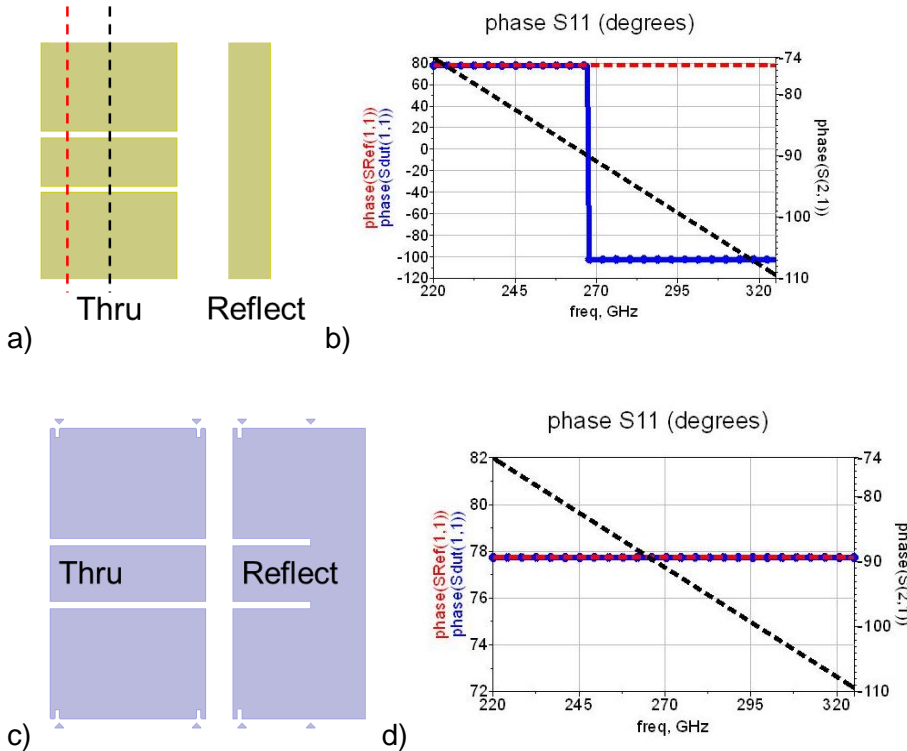


Fig. 35: Layout and simulated response of flush (a-b) and offset short (c-d), showing the phase error that can occur when the electrical length between the centre of the thru and the intrinsic short location is larger than $\lambda/8$.

Guideline #8

When designing custom kits for LRM/TRL calibration the reflect should be realized as an offset one, keeping the minimum distance between the effective reflect and the center of the thru line (intrinsic calibration plane) to avoid requiring sign changes in the solution of the calibration equations.

Three transmission lines with lengths of 360, 450 and 680 μm are fabricated to allow single line TRL calibration in the WR3, WR5 and WR10 waveguide bands, respectively. Finally, a 600 μm long CPWG is used for calibration verification. The first two metal layers of the BEOL have been used to realize a meshed ground plane satisfying the metal density rules. The bottom ground plane is electrically connected to the coplanar ground planes using interleaved meshed metal on all layers and employing the maximum via density allowed. The CPW line is 30 μm wide and 3 μm thick with a 10 μm gap (Fig. 34 d). The silicon dioxide acting as a dielectric has a relative permittivity of ca. 4.1, almost homogeneously among the entire structure, allowing simple simulation geometry. The quality of the calibration achieved by the custom designed TRL kit, was benchmarked using the worst case bound metric using the 600 μm long CPWG as the verification structure. To normalize the S-parameter to the system impedance (i.e., 50Ohm) one of the methods advised in guideline #3 (i.e., 3D EM FEM solver) and the calibration comparison method from [14] were employed. The result is shown in Fig. 36.

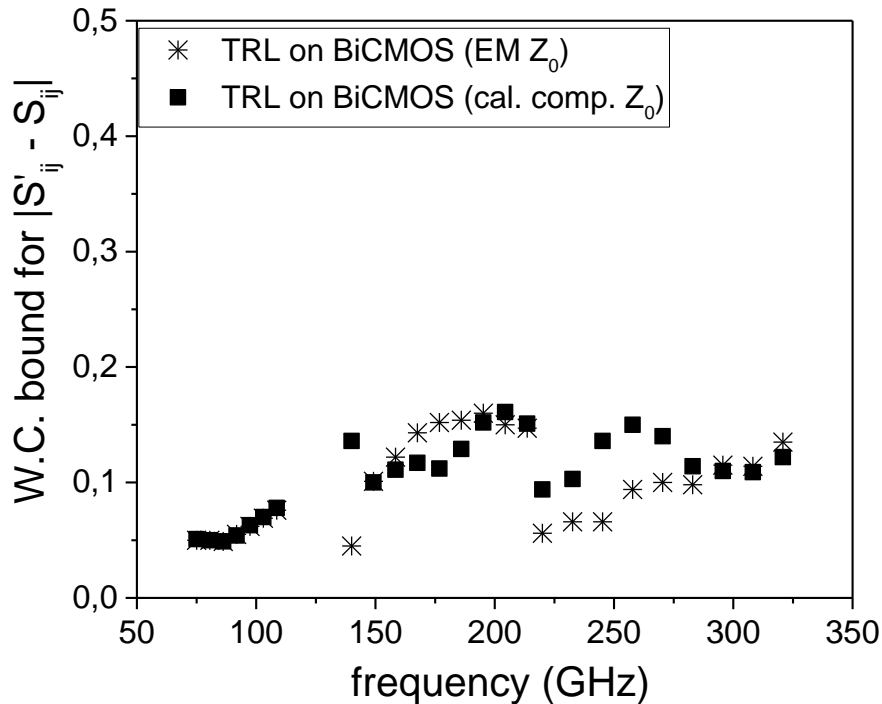


Fig. 36: Comparison of probe-tips corrected measurements of a verification line manufactured on the SiGe BEOL in the frequency range 75-325 GHz.

Acknowledgements

The authors acknowledge support by the European Metrology Programme for Innovation and Research (EMPIR) Project 14IND02 "Microwave measurements for planar circuits and components". The EMPIR program is co-financed by the participating countries and from the European Union's Horizon 2020 research and innovation program.

Bibliography

- [1] Douglas K. Rytting, "Network Analyzer Error Models and Calibration Methods," 62nd ARFTG Conference Short Course Notes, December 2-5, 2003, Boulder, CO.
- [2] L. Galatro, A. Pawlak, M. Schroter and M. Spirito, "Capacitively Loaded Inverted CPWs for Distributed TRL-Based De-Embedding at (Sub) mm-Waves," in IEEE Transactions on Microwave Theory and Techniques, vol. 65, no. 12, pp. 4914-4924, Dec. 2017.
- [3] Davidson, K. Jones, and E. Strid, "LRM and LRRM Calibrations with Automatic Determination of Load Inductance," in ARFTG Conf. Dig, Monterey, CA, USA, 1990, pp. 57-63.
- [4] G. F. Engen and C. A. Hoer, "Thru-Reflect-Line: An Improved Technique for Calibrating the Dual Six-Port Automatic Network Analyzer," IEEE Trans. Microw. Theory Techn., vol. 27, no. 12, pp. 987-993, Dec. 1979.
- [5] L. Galatro and M. Spirito, "Millimeter-Wave On-Wafer TRL Calibration Employing 3-D EM Simulation-Based Characteristic Impedance Extraction," in IEEE Transactions on Microwave Theory and Techniques, vol. 65, no. 4, pp. 1315-1323, April 2017. doi: 10.1109/TMTT.2016.2609413.
- [6] R. Simons, "Coplanar Waveguide Discontinuities and Circuit Elements," in Coplanar Waveguide Circuits, Components, and Systems, Wiley-IEEE Press, 2001, pp. 237-287.

- [7] N. K. Das, "Spectral-domain analysis of complex characteristic impedance of a leaky conductor-backed slotline," 1996 IEEE MTT-S International Microwave Symposium Digest, San Francisco, CA, USA, 1996, pp. 1791-1794 vol.3. doi: 10.1109/MWSYM.1996.512291.
- [8] F. Schnieder, T. Tischler and W. Heinrich, "Modeling dispersion and radiation characteristics of conductor-backed CPW with finite ground width," in IEEE Transactions on Microwave Theory and Techniques, vol. 51, no. 1, pp. 137-143, Jan 2003.
- [9] D. Williams and R. B. Marks, "Calibrating On-Wafer Probes to the Probe Tips," ARFTG Conf. Dig, vol. 22, pp. 136-143, Dec. 1992.
- [10] G. Gold and K. Helmreich, "A Physical Surface Roughness Model and Its Applications," IEEE Trans. Microw. Theory Techn., vol. PP, no. 99, pp. 1–13, 2017, doi: 10.1109/TMTT.2017.
- [11] S. L. van Berkel, A. Garufo, N. Lombart and A. Neto, "A Quasi-Analytical Tool for the Characterization of Transmission Lines at High Frequencies [EM Programmer's Notebook]," in IEEE Antennas and Propagation Magazine, vol. 58, no. 3, pp. 82-90, June 2016. doi: 10.1109/MAP.2016.2541617.
- [12] D. F. Williams, F. J. Schmückle, R. Doerner, G. N. Phung, U. Arz, and W. Heinrich, "Crosstalk Corrections for Coplanar –Waveguide Scattering-Parameter Calibrations," IEEE Trans. Microw. Theory Tech., vol. 62, no. 8, pp. 1748-1761, Aug. 2014.
- [13] T. K. Johansen, C. Jiang, D. Hadziabdic, and V. Krozer, "EM Simulation Accuracy Enhancement for Broadband Modeling of On-Wafer Passive Components," in Proc. of the 37th European *Microwave Integrated Circuit Conference* (EuMIC), Munich, Germany, Oct. 2007, pp. 1245-1248.
- [14] D. Williams, U. Arz, and H. Grabinski, "Accurate characteristic impedance measurement on silicon," IEEE MTT-S Int. Microw. Symp. Dig., Baltimore, MD, USA, 1998, pp. 155-158.